

Controls of Atmospheric Methane on Early Earth and Inhabited Earth-like Terrestrial Exoplanets

Aika Akahori¹, Yasuto Watanabe^{1,2*}, Eiichi Tajika¹

Abstract

Methane (CH₄) is a primarily biogenic greenhouse gas. As such, it represents an essential biosignature to search for life on exoplanets. Atmospheric CH₄ abundance on Earth-like inhabited exoplanets is likely controlled by marine biogenic production and atmospheric photochemical consumption. Such interactions have been previously examined for the case of the early Earth where primitive marine ecosystems supplied CH₄ to the atmosphere, showing that the atmospheric CH₄ response to biogenic CH₄ flux variations is nonlinear, a critical property when assessing CH₄ reliability as a biosignature. However, the contributions of atmospheric photochemistry, metabolic reactions, or solar irradiance to this nonlinear response are not well understood. Using an atmospheric photochemical model and a marine microbial ecosystem model, we show that production of hydroxyl radicals from water vapor photodissociation is a critical factor controlling the atmospheric CH₄ abundance. Consequently, atmospheric CH₄ partial pressure ($p\text{CH}_4$) on inhabited Earth-like exoplanets orbiting Sun-like stars (F-, G-, and K-type stars) would be controlled primarily by stellar irradiance. Specifically, irradiance at wavelengths of approximately 200–210 nm is a major controlling factor for atmospheric $p\text{CH}_4$ when the carbon dioxide partial pressure is sufficiently high to absorb most stellar irradiance at 170–200 nm. Finally, we also demonstrated that inhabited exoplanets orbiting near the outer edge of K-type stars' habitable zones are better suited for atmospheric $p\text{CH}_4$ buildup. Such properties will valuably support future detection of life signatures.

¹ Department of Earth and Planetary Science, The University of Tokyo, Hongo 7-3-1, Bunkyo-ku, Tokyo, Japan. 113-0033

² Meteorological Research Institute, Japan Meteorological Agency, Nagamine 1-1, Tsukuba, Ibaraki, Japan. 305-0052

* Corresponding Author yasuto.watanabe.wess@gmail.com

1. INTRODUCTION

Solar luminosity on early Earth during the Hadean (> 4.0 Ga) and Archean (4.0–2.5 Ga) was ~ 70 –80% of its current value (Gough 1981). Even under such young Sun conditions, early Earth was maintained habitable by the presence of liquid water at its surface (Sagan and Mullen 1972; Mojzsis et al. 2001; Wilde et al. 2001; Feulner 2012; Catling and Zahnle 2020), ensured by elevated concentrations of greenhouse gases, the major contributors to early-Earth warming mechanisms (Sagan and Mullen 1972; Walker et al. 1981; Sagan and Chyba 1997; Haqq-Misra et al. 2008; Goldblatt and Zahnle 2011; Wordsworth and Pierrehumbert 2013). Carbon dioxide (CO_2) is one of the most fundamental greenhouse gasses in planetary atmospheres, with estimated early-Earth concentrations approximately 100 to 1000 times larger than the preindustrial reference value (Tajika and Matsui 1992; Kasting 1993; Krissansen-Totton et al. 2018; Isson and Planavsky 2018; Kadoya et al. 2020). Methane (CH_4), the second most abundant greenhouse gas in the current atmosphere, was initially produced and emitted into the early-Earth atmosphere by a primitive marine microbial ecosystem (Kiehl and Dickinson 1987; Pavlov et al. 2001; Kasting 2005; Haqq-Misra et al. 2008; Ozaki et al. 2018). The first living organisms emerged during the Hadean or early Archean (4.0–3.5 Ga), less than 1 Gyr after the Earth formed (Lazcano and Miller 1994; Chyba and McDonald 1995; Ueno et al. 2006; Dodd et al. 2017; Tashiro et al. 2017; Pearce et al. 2018). Moreover, methanogens, microorganisms that produce CH_4 by decomposing organic matter, probably emerged nearly simultaneously, during the early to middle Archean (Battistuzzi et al. 2004; Ueno et al. 2006; Wolfe and Fournier 2018). Although CH_4 is less abundant than CO_2 on current Earth, it is also a considerably more potent greenhouse gas. Therefore, the emergence of life may have fundamentally influenced the early atmospheric composition. Theoretical studies

have suggested that biogenic CH₄ accumulated in the early atmosphere, warming the Earth surface (Pavlov et al. 2001; Ozaki et al. 2018).

Relationships between the atmosphere and marine microbial ecosystem activity on early Earth are particularly interesting in relation to the investigation of exoplanetary atmospheres. Because early CH₄ sources, as on Earth currently, were probably exclusively biological, CH₄ is also considered a potentially strong biosignature detectable from inhabited Earth-like exoplanets (Schindler and Kasting 2000; Kasting and Catling 2003; Catling et al. 2018; Wogan and Catling 2020; Wogan et al. 2020; Sauterey et al. 2020; Krissansen-Totton et al. 2022; Thompson et al. 2022). Concentrations of atmospheric biogenic gases respond nonlinearly to reducing-gas outgassing flux through changes in atmospheric photochemical reaction rates (Pavlov et al. 2003; Kasting 2005; Ozaki et al. 2018; Ranjan et al. 2022; Watanabe et al. 2023b). Therefore, understanding the response of atmospheric photochemical reactions to biological activity is essential to understand early-Earth evolution of the atmosphere and biosphere and to assess the potential role of CH₄ as a biosignature on exoplanets.

Using a coupled model that couples atmospheric photochemistry with a primitive marine microbial ecosystem (Figure 1), a previous study demonstrated that the high atmospheric CH₄ partial pressure ($p\text{CH}_4$) required to sustain warm climate conditions, within an estimated atmospheric CO₂ level ($p\text{CO}_2$) range representative of the mid-Archean, could be produced by the nonlinear response of atmospheric $p\text{CH}_4$ to primitive marine biospheric activities (Figure 1) (Ozaki et al. 2018). The primary production in the primitive marine microbial ecosystem was mainly due to anoxygenic photoautotrophs (AP), organisms that perform photosynthesis without producing oxygen using electron donors such as hydrogen (H₂) and ferrous iron (Fe(II)) (Kharecha et al. 2005; Canfield et al. 2006; Ozaki et al. 2018; Ward et al. 2019). This leads to an increase in biogenic CH₄

production rate and atmospheric $p\text{CH}_4$ by enhancing the activity of methanogenesis. Another plausible source of CH_4 on early Earth was the activity of chemoautotrophs, which utilize carbon monoxide (CO) as an electron donor (CO-consuming chemoautotroph; CO-C) (Ragsdale 2004; Kharecha et al. 2005; Ozaki et al. 2018; Schwieterman et al. 2019; Watanabe et al. 2023b). However, possible causes for nonlinearity of the atmospheric $p\text{CH}_4$ response, in terms of interactions between metabolic pathways and atmospheric composition, have not been systematically assessed. Specifically, the roles of the nonlinear patterns of CH_4 and the influence of solar irradiance on atmospheric photochemical reactions, also critical to analyzing exoplanetary atmospheres, remain unclear. In this study, we use an atmospheric photochemical model and a marine microbial ecosystem model to investigate possible factors controlling CH_4 abundance in the early-Earth atmosphere and on Earth-like inhabited exoplanets in orbit around F-, G-, and K-type central stars.

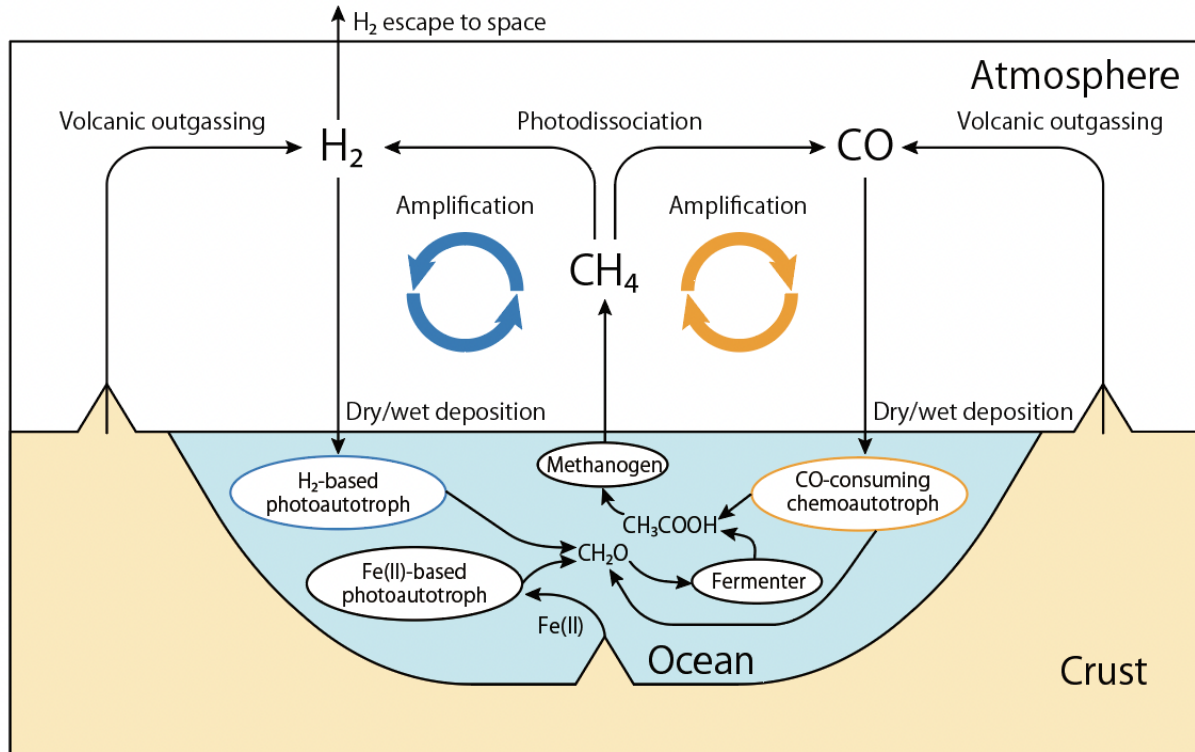


Figure 1. Schematic illustration of the interactions of atmospheric photochemistry and marine microbial ecosystem on early Earth based on Ozaki et al. (2018).

2. METHODS

2.1. Coupled Model for Atmospheric Photochemistry and Marine Microbial Ecosystems

We used the coupled model for atmospheric photochemistry and marine microbial ecosystems that includes the 1D photochemical model “Atmos” (Arney et al. 2016, 2017, 2018) and the primitive marine microbial ecosystem model (Ozaki et al. 2018; Watanabe et al. 2023b). The photochemical model version; lower boundary conditions; absorption cross-sections (Figure A1) (Ranjan et al. 2020); and vertical profiles of atmospheric number density, temperature, and eddy diffusion coefficient were identical to those used in Watanabe et al. (2023b).

The ecosystem model is similar to the earlier model of Ozaki et al. (2018), but with an improved formulation (Watanabe et al. 2023b). Biological reactions implemented in the model are summarized in Table 1. They describe the activity of H₂-based and Fe(II)-based AP (hereafter H₂-AP and Fe-AP, respectively), CO-C, fermenters, and methanogens. In this study, we assumed two types of primitive marine microbial ecosystems (Ozaki et al., 2018), differing by the omission (Type I ecosystem) or inclusion (Type II ecosystem) of Fe-AP activity and ferric iron (Fe(III)) reduction (Table 1). The CH₄ flux from the ocean into the atmosphere, $\Phi_{\uparrow}(\text{CH}_4)$, is expressed as (Kharecha et al. 2005; Ozaki et al. 2018; Watanabe et al. 2023b):

$$\begin{aligned} \Phi_{\uparrow}(\text{CH}_4) &= \frac{1}{2}(1 - \beta_{bur}) \cdot F_{npp} + \frac{1-g_{co}}{4-2g_{co}} \Phi_{\downarrow}(\text{CO}) + \Phi_{\downarrow}(\text{CH}_4) && \text{(Type I),} \\ &= \frac{1}{2}(1 - \beta_{bur}) \cdot F_{npp} + \frac{1-g_{co}}{4-2g_{co}} \Phi_{\downarrow}(\text{CO}) - \frac{\gamma_{red}}{8} \Phi_{\uparrow}(\text{Fe(II)}) + \Phi_{\downarrow}(\text{CH}_4) && \text{(Type II), (1)} \end{aligned}$$

where $\Phi_{\downarrow}(\text{CO})$ and $\Phi_{\downarrow}(\text{CH}_4)$ are the total deposition rates (sum of the dry and wet deposition rates) of CO and CH₄, respectively; β_{bur} is the organic carbon burial efficiency, F_{npp} is the net primary productivity of the anaerobic marine ecosystem; g_{co} is the growth yield of CO-C; γ_{red} is the iron reduction efficiency, and $\Phi_{\uparrow}(\text{Fe(II)})$ is the rate of Fe(II) upwelling from the deep ocean to the euphotic zone. The standard parameters are summarized in Tables 2 and 3. We assumed that the

primitive marine ecosystem productivity is limited by the electron donors supply rate. Thus, F_{npp} is expressed as:

$$F_{npp} = \frac{1}{2}\Phi_{\downarrow}(H_2) + \frac{g_{co}}{4-2g_{co}}\Phi_{\downarrow}(CO) \quad (\text{type I})$$

$$= \frac{1}{2}\Phi_{\downarrow}(H_2) + \frac{1}{4}\Phi_{\uparrow}(Fe^{II}) + \frac{g_{co}}{4-2g_{co}}\Phi_{\downarrow}(CO) \quad (\text{type II}) \quad (2)$$

where $\Phi_{\downarrow}(H_2)$ is the H_2 surface removal flux (sum of the dry and wet deposition fluxes).

Table 1. List of biological reactions. g_{co} is the growth yield of CO-consuming chemoautotroph.

Note, the reaction B6 is included in the model but its activity is set to zero in this study.

#	Reaction	Reaction	Type I	Type II
B1	H_2 -based anoxygenic photosynthesis	$2H_2 + CO_2 + hv \rightarrow CH_2O + H_2O$	✓	✓
B2	Fe(II)-based anoxygenic photosynthesis	$4Fe^{2+} + 11H_2O + CO_2 + hv \rightarrow CH_2O + 8H^+$		✓
B3	CO-consuming chemoautotroph	$(4 - 2g_{co}) \cdot CO + (2 - g_{co}) \cdot H_2O$ $\rightarrow g_{co} \cdot CH_2O + (2 - g_{co}) \cdot CO_2 + (1 - g_{co}) \cdot CH_3COOH$	✓	✓
B4	Fermenter	$2CH_2O \rightarrow CH_3COOH$	✓	✓
B5	Methanogen	$CH_3COOH \rightarrow CH_4 + CO_2$	✓	✓
B6	Fe(III) reduction	$CH_3COOH + 8Fe(OH)_3 + 16H^+ \rightarrow 8Fe^{2+} + 22H_2O + 2CO_2$		✓

Once the model reaches steady state, the net oxidizing and reducing power supply rates into the ocean–atmosphere system become balanced. The model global redox budget then becomes (Holland 1984; Canfield et al. 2006; Ozaki et al. 2018; Watanabe et al. 2023b):

$$F_{volc,red} + 0.5F_{Fe(III)} = F_{esc,H_2} + 2F_{bur,oc} + \Sigma\Delta\Phi_{red} \quad (3)$$

where $F_{volc,red}$ is the volcanic outgassing rate for reduced gases, $F_{Fe(III)}$ is the Fe(III) deposition rate from the ocean, F_{esc,H_2} is the H₂ escape rate to space, $F_{bur,oc}$ is the organic carbon burial rate from the ocean, and $\Sigma\Delta\Phi_{red}$ is a residual term that represents the net removal rate of reducing power (converted into units of H₂ reducing power) via deposition of atmospheric chemical species (Watanabe et al. 2023b). The left-hand side in equation (3) represents the reducing power supply rate (oxidizing power removal rate). Conversely, the right-hand side represents the oxidizing power supply rate (reducing power removal rate). The term $F_{volc,red}$ is expressed as the sum of H₂, CO, and hydrogen sulfide (H₂S) outgassing fluxes ($\Phi_{\uparrow}(H_2)$, $\Phi_{\uparrow}(CO)$, and $\Phi_{\uparrow}(H_2S)$, respectively):

$$F_{volc,red} = \Phi_{\uparrow}(H_2) + \Phi_{\uparrow}(CO) + 3\Phi_{\uparrow}(H_2S), \quad (4)$$

where the multiplying factor for $\Phi_{\uparrow}(H_2S)$ is required for unit conversion to the reducing power equivalent to H₂. The outgassing rates in all simulations are summarized in Tables 2 and 3. We did not consider CH₄ abiotic outgassing flux because it is much smaller than the biogenic flux (Thompson et al. 2022). In these conditions, the atmospheric redox budget becomes:

$$F_{volc,red} + 4\Phi_{\uparrow}(CH_4) = F_{esc,H_2} + \Sigma\Delta\Phi_{red} \quad (5)$$

From equation (5), we infer that the increase in reducing power supply rate to the atmosphere provided by biogenic CH₄ is compensated (removed from the atmosphere) through both escape of H₂ to space and deposition of reducing chemical species from the atmosphere into the ocean.

Table 2. List of the standard parameters adopted in this study.

Parameter	Label	Value	Unit	Remarks and Reference
Atmospheric $p\text{CO}_2$	$p\text{CO}_2$	0.03 (Archean Earth) 0.1 (F-, G-, and K-type)	bar	–
Stellar irradiance (present Earth = 1)	S^*	0.8 (Archean Earth) 1.0 (F-, G-, and K-type)	–	(Gough, 1981)
Volcanic outgassing rate of H_2	$\Phi_{\text{out}}(\text{H}_2)$	2.7	$\text{Tmol H}_2 \text{ yr}^{-1}$	(Catling and Kasting 2017; Ozaki et al. 2018)
Volcanic outgassing rate of H_2S	$\Phi_{\text{out}}(\text{H}_2\text{S})$	0.0945	Tmol S yr^{-1}	(Wogan and Catling 2020; Watanabe et al. 2023b)
Fraction of Fe(III) decomposed by Fe(III)-reducing bacteria	r_{ferred}	0	–	(Ozaki et al., 2018)
Burial efficiency of organic carbon	β_{bur}	0.02	–	(Betts and Holland 1991; Ozaki et al. 2018)
Growth yield of the CO-consuming chemoautotroph	g_{co}	0.1	–	(Kharecha et al. 2005; Watanabe et al. 2023b)
Unit conversion factor from $\text{cm}^{-2} \text{ s}^{-1}$ to Tmol yr^{-1}	–	270	–	–

Table 3. List of numerical experiments conducted in this study.

Experiment name	$\Phi_i(\text{H}_2)$ ($\text{cm}^{-2} \text{s}^{-1}$)	$\Phi_i(\text{CO})$ ($\text{cm}^{-2} \text{s}^{-1}$)	$\Phi_i(\text{Fe(II)})$ ($\text{cm}^{-2} \text{s}^{-1}$)	$\Phi_i(\text{CH}_4)$ ($\text{cm}^{-2} \text{s}^{-1}$)	$p\text{CO}_2$ (bar)	Stellar Spectrum	Remarks
<i>ExpH2outgassTypeI</i>	1×10^8 – 3×10^{11}	0	N/A	N/A	0.03	Early Sun (2.8 Ga) G-type (Sun)	No Fe(II)-based anoxygenic photoautotroph Ozaki et al. (2018) equivalent
<i>ExpH2outgassTypeII</i>	1×10^8 – 3×10^{11}	0	3×10^{11}	N/A	0.03	Early Sun (2.8 Ga)	Ozaki et al. (2018) equivalent
<i>ExpCOoutgassTypeI</i>	1×10^{10}	1×10^8 – 3×10^{11}	N/A	N/A	0.03	Early Sun (2.8 Ga)	No Fe(II)-based anoxygenic photoautotroph
<i>ExpCH4flux</i>	1×10^{10}	0	N/A	1×10^6 – 9×10^{11}	0.001 0.003 0.01 0.03 0.1 0.342 1.2	Early Sun (2.8 Ga)	–
<i>ExpCH4fluxG2V</i>	1×10^{10}	0	N/A	1×10^6 – 9×10^{11}	0.001 0.01 0.1	G-type (Sun)	–
<i>ExpCH4fluxF2V</i>	1×10^{10}	0	N/A	1×10^6 – 9×10^{11}	0.001 0.01 0.1	F-type (σ -Bootis)	–
<i>ExpCH4fluxK2V</i>	1×10^{10}	0	N/A	1×10^6 – 9×10^{11}	0.001 0.01 0.1	K-type (ϵ -Eridani)	–
<i>ExpCH4flux200nm</i>	1×10^{10}	0	N/A	1×10^6 – 9×10^{11}	0.1	G-type (Sun) but irradiance at 200–210 nm is scaled by 0.1, 0.5, 1, 2, 10, or 40.	–
<i>ExpIrradiance</i>	1×10^{10}	0	N/A	1×10^9 3×10^9 1×10^{10} 3×10^{10} 1×10^{11}	0.1	G-type (Sun) scaled by 0.2–1.2	–

2.2. Experimental Setup

We first conducted two sets of simulations similar to those of Ozaki et al. (2018): one set for a Type I ecosystem including H₂-AP, CO-C, and decomposers, but without Fe-AP (Table 3, *ExpH2outgassTypeI*) and another set for a Type II ecosystem including H₂-AP, Fe-AP, CO-C, and decomposers (Table 3, *ExpH2outgassTypeII*). In each set, we conducted simulations with respect to a different H₂ outgassing rate value (from 1×10^8 to 3×10^{11} cm⁻² s⁻¹). In addition, we also conducted an additional sensitivity test to the CO outgassing flux for the Type I ecosystem (Table 3, *ExpCOoutgassTypeI*). These simulations were conducted with a fixed atmospheric *p*CO₂ of 0.03 bar (Table 3), a reasonable value for late Archean conditions (Kanzaki and Murakami 2015; Ozaki et al. 2018).

Then, we conducted additional sensitivity tests to assess the influence of the CH₄ flux from the ocean into the atmosphere (from 1×10^6 to 9×10^{11} cm⁻² s⁻¹) on the atmospheric composition (Table 3, *ExpCH4flux*). These simulations used the same photochemical model decoupled from the ecosystem model, allowing us to assess the atmospheric response to a broader range of CH₄ fluxes than with using the coupled model. This set of simulations was repeated for different values of atmospheric *p*CO₂ (0.001, 0.003, 0.01, 0.03, 0.1, 0.342, and 1.2 bar). Total atmospheric pressure was adjusted when atmospheric *p*CO₂ was larger than 0.2 bar (Watanabe and Ozaki 2023). The H₂ outgassing rate was set to 10^{10} cm⁻² s⁻¹. Solar luminosity was set to ~ 0.8 times its current value, representative of “young Sun” conditions (2.8 Ga).

Finally, we conducted three sets of simulations for central stars of F, G, and K types (Table 3, *ExpCH4fluxF2V*, *ExpCH4fluxG2V*, and *ExpCH4fluxK2V*, respectively), with three settings in each case for the atmospheric *p*CO₂ values of 0.001, 0.01, and 0.1 bar. The adopted irradiance spectra (Figure 2) were those of σ Bootis for F-type stars (Segura et al. 2003), the current Sun for

G-type stars (Thuillier et al., 2004), and ϵ Eridani for K-type stars (Segura et al. 2003). All spectra were scaled so that stellar irradiance at the top of the exoplanetary atmosphere is equal to the solar value on current Earth. We conducted further simulations for a G-type star (current Sun), but with (1) irradiance at wavelengths within $\sim 200\text{--}210$ nm scaled successively by a factor of 0.1, 0.5, 1, 2, 10, and 40 (Table 3, *ExpCH4flux200nm*); and (2) with finer solar irradiance scaling at all wavelengths (factor of 0.2–1.2; Table 3, *ExpIrradiance*). The irradiance scaling range in (2) is sufficient to represent expected conditions within the habitable zone of G-type stars, defined as the circumstellar region where a terrestrial planet with an atmospheric composition including mainly CO₂, water vapor (H₂O), and nitrogen (N₂) can sustain liquid water at its surface (Kasting et al. 1993; Selsis et al. 2007; Kopparapu et al. 2013, 2014). For the current Sun, the habitable zone limits are estimated to be $\sim 0.99\text{--}1.70$ au, corresponding to stellar irradiances of $\sim 1.01\text{--}0.35$ times that of Earth (Kopparapu et al. 2013). Both sets of simulations were repeated for five distinct CH₄ flux values (1×10^9 , 3×10^9 , 1×10^{10} , 3×10^{10} , and 1×10^{11} cm⁻² s⁻¹).

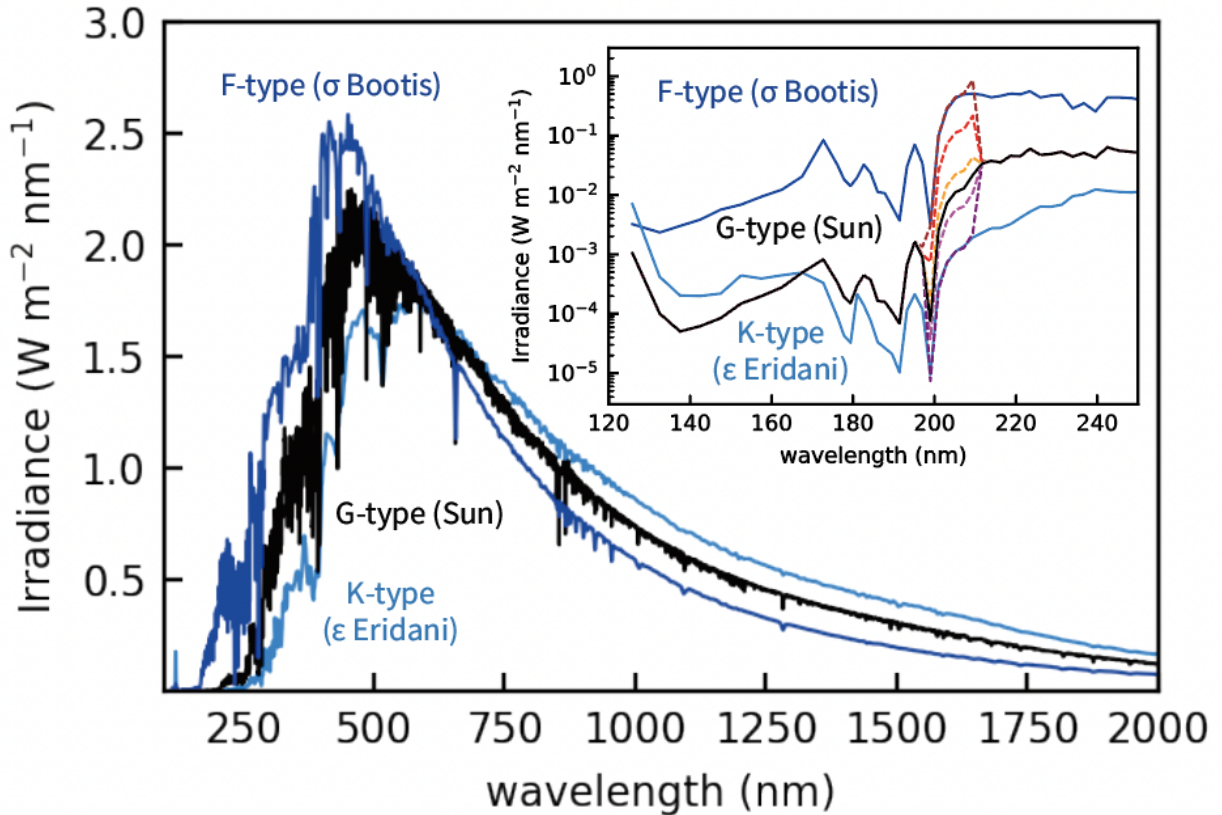


Figure 2. Spectrum of the radiation of the Sun-like stars (F-, G-, and K-type stars) employed in this study (blue, black, and light blue lines, respectively) (Segura et al., 2003; Thuillier et al., 2004). This original spectrum is translated into the model grid in wavelength and used as an input of the model. The upper-right window shows the ultraviolet region of the radiation spectrum that is translated into the model wavelength grid. The solid lines are the input spectrum of F-, G-, and K-type stars (blue, black, and light blue lines, respectively). The dashed lines represent the spectra of the G-type star, which are scaled 0.1, 0.5, 2, 10, and 40 times at 200–210 nm (purple, light purple, orange, red, and brown lines, respectively).

3. RESULTS

3.1. Global Redox Budget and CH₄ Amplification on Early Earth

Simulation results reproducing the study of Ozaki et al. (2018) are shown in Figure 3. The current coupled model version correctly reproduced the nonlinear response of atmospheric $p\text{CH}_4$ to H₂ outgassing rate variations. As discussed by Ozaki et al. (2018), calculated atmospheric $p\text{CH}_4$ was larger than 0.001 bar for Type II ecosystems (active Fe-AP; red lines in Figure 3), independently of the H₂ outgassing rate, but depended strongly on it for Type I ecosystems (black lines in Figure 3). This indicates nonlinear amplification of atmospheric $p\text{CH}_4$ for high Fe-AP activity, easily explained by analyzing the global redox budget. In Figures 3b, 3d, and 3f, the result is shown as a function of the influx of reducing power (equation (2), left-hand side). For Type II ecosystems, the electron donors supply rate was always larger than 40 Tmol H₂ eq. yr⁻¹ because of the high Fe(II) upwelling rate (~80 Tmol Fe yr⁻¹; red line in Figure 3b). This clearly demonstrates that the influx of reducing power (i.e., global redox budget) controls the primitive marine biosphere activity, thus atmospheric $p\text{CH}_4$. When the influx of reducing power exceeds ~60 Tmol H₂ eq. yr⁻¹, CH₄ decreases slightly, whereas atmospheric $p\text{CH}_4$ increases. For a reducing power influx higher than this threshold, hydrocarbon haze, composed of hydrocarbon aerosols, forms in the atmosphere and affect CH₄ chemistry (Sagan and Chyba 1997; Pavlov et al. 2001; Arney et al. 2016). However, investigating hydrocarbon haze requires the consideration of temperature profile changes (Arney et al. 2016, 2017), so it is beyond the scope of this study. For this reason, we analyze the response of atmospheric $p\text{CH}_4$ when the atmospheric haze layer is not formed.

For simulated Type I ecosystems, increased H₂ outgassing flux (i.e., influx of reducing power) enhanced the H₂-AP activity. Consequently, both the biogenic CH₄ production rate and the atmospheric $p\text{CH}_4$ increases (Figure 3b). This implies that early-Earth atmospheric $p\text{CH}_4$ was

determined by interactions between the atmosphere and the marine biosphere in response to an influx of reducing power to the ocean–atmosphere system. For this reason, in Type-I ecosystems, we focus on the relationships between the influx of reducing powers, $\Phi_{\uparrow}(\text{CH}_4)$, and atmospheric $p\text{CH}_4$.

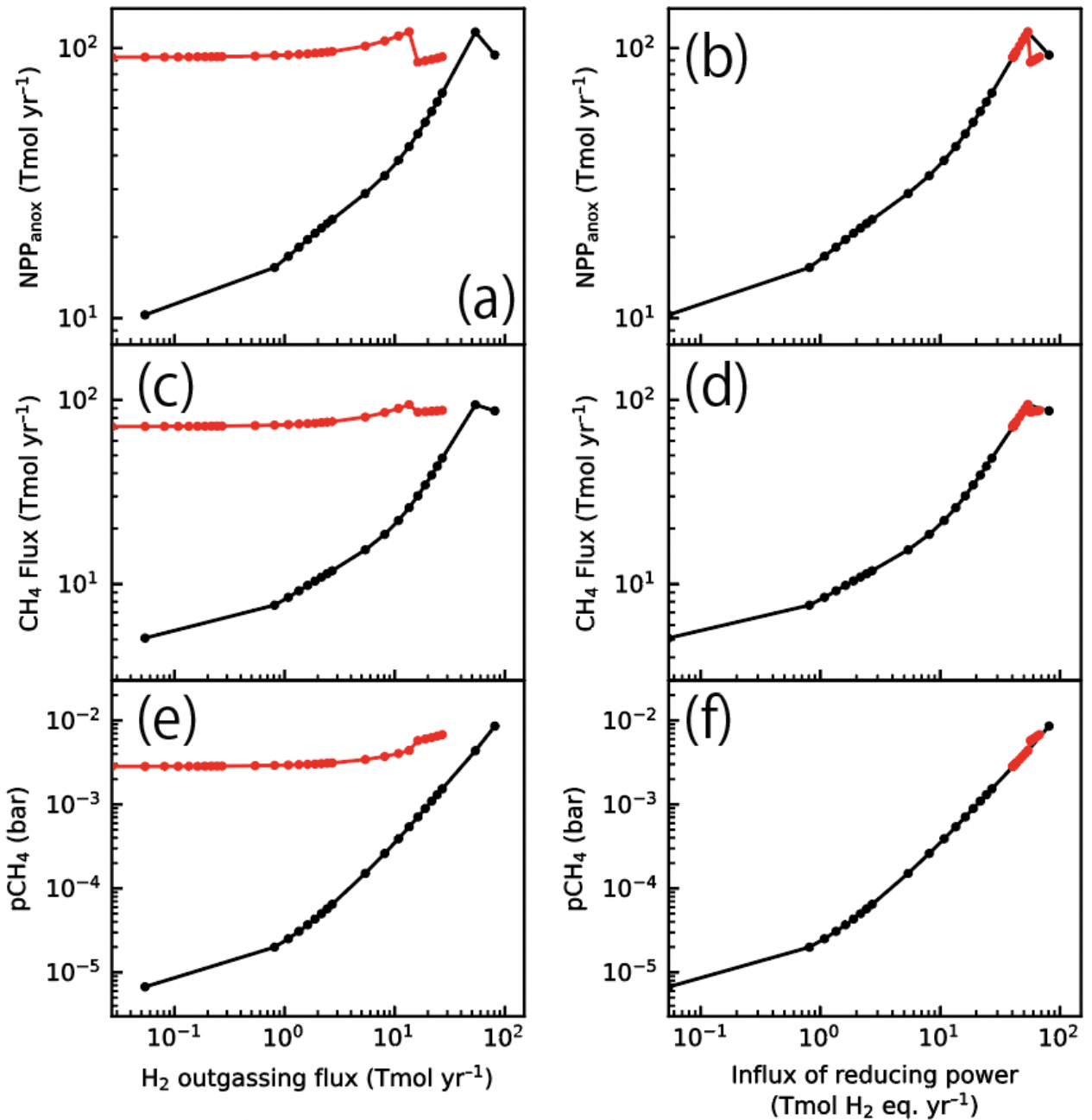


Figure 3. Response of primary productivity (a, b), biogenic CH_4 flux (c, d), and atmospheric $p\text{CH}_4$ in response to the changes in the outgassing flux of H_2 (a, c, e) and the influx of reducing power (left-hand side of equation (5)) (b, d, f), which are equivalent to the results in Ozaki et al. (2018). The black lines represent the result with H_2 -based anoxygenic photoautotrophs (APs) but without Fe(II)-based APs (*ExpH2outgassTypeI* in Table 3). The red lines represent the result with H_2 -using AP and Fe(II)-based AP, assuming the Fe(II) upwelling rate is approximately $80 \text{ Tmol Fe yr}^{-1}$ (*ExpH2outgassTypeII* in Table 3).

3.2. Response of the Biogenic CH₄ Supply Rate to H₂ and CO Outgassing Rate Variations

CH₄ flux amplification related to reducing gas outgassing (i.e., the influx of reducing power) occurs through two main pathways: recycling of atmospheric H₂ and CO by H₂-AP and CO-C, respectively (Figure 1). Responses of atmospheric $p\text{CH}_4$, CO partial pressure ($p\text{CO}$), and H₂ partial pressure ($p\text{H}_2$) to $\Phi_{\uparrow}(\text{CH}_4)$ are illustrated in Figure 4. Atmospheric $p\text{CH}_4$ and $p\text{CO}$ increase nonlinearly with increasing $\Phi_{\uparrow}(\text{CH}_4)$, whereas $p\text{H}_2$ exhibits a nearly linear dependence on the CH₄ flux (Figure 4c). When the CH₄ flux increases, the CO consumption flux via reaction with hydroxyl (OH) radicals (reaction (R1)) decreases rapidly below approximately 40 km (Figure 5b and 5c).



This decrease is explained by OH consumption by biogenic CH₄ when the H₂ outgassing rate is high (Figure 5e):



This causes a sharp increase in the wet and dry deposition rate of CO to the ocean and in the activity of CO-C. As a result, the CH₄ production rate increases, further enhancing CO production. We repeated this simulation with different CO outgassing fluxes to confirm the dependence of the H₂ and CO budgets on volcanic gas composition (Table 3, *ExpCOoutgassTypeI*). Results were similar to those obtained for different H₂ outgassing fluxes (Figures 4b and 4c). Therefore, the nonlinear responses of both the electron donors supply rate and $\Phi_{\uparrow}(\text{CH}_4)$ were primarily caused by abundance variations of CO, CH₄, and OH radicals.

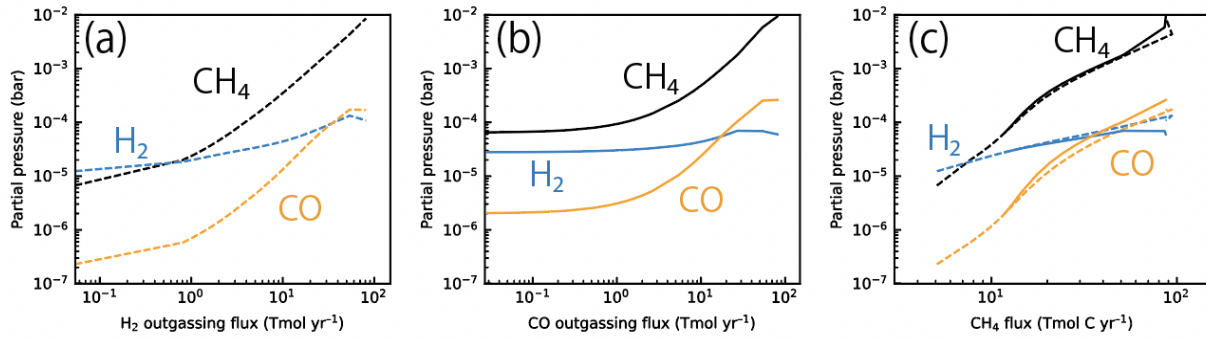


Figure 4. Response of the atmospheric $p\text{CH}_4$, $p\text{H}_2$, and $p\text{CO}$ (black, blue, and orange lines, respectively) to the change in H_2 outgassing flux (a), CO outgassing flux (b), and the biogenic CH_4 flux (c). Calculations are conducted with atmospheric $p\text{CO}_2$ of 0.03 bar (*ExpH2outgassType1* and *ExpCOoutgassType1* in Table 3). The dashed line represents the results with different H_2 outgassing fluxes. The solid line represents the results with different CO outgassing fluxes.

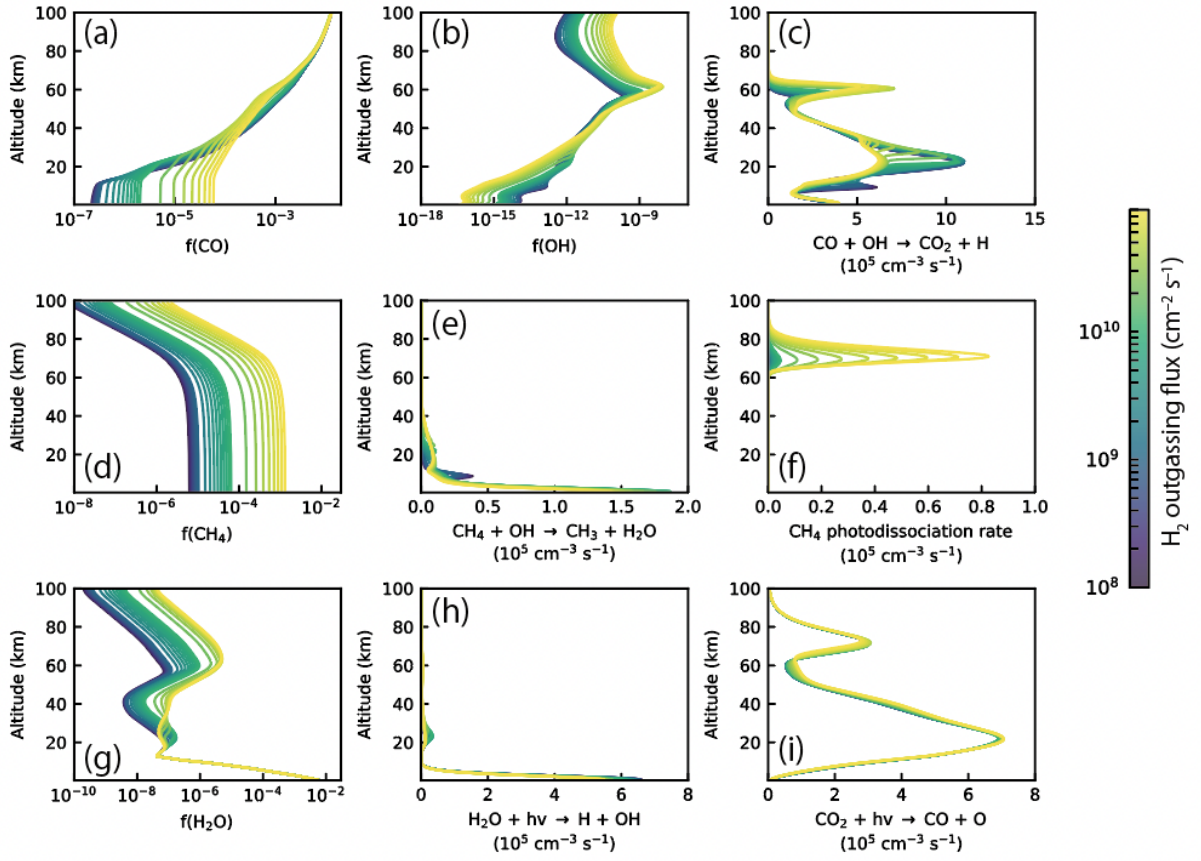


Figure 5. Vertical profiles of the atmospheric components and the reaction rates. Vertical profiles of (a) CO mixing ratio, (b) OH radical mixing ratio, (c) reaction rate of $\text{CO} + \text{OH} \rightarrow \text{CO}_2 + \text{H}$, (d) CH_4 mixing ratio, reaction rate of (e) $\text{CH}_4 + \text{OH} \rightarrow \text{CH}_3 + \text{H}_2\text{O}$, (f) photodissociation rate of CH_4 , (g) H_2O mixing ratio, (h) photodissociation rate of H_2O , and (i) photodissociation rate of CO_2 . Calculations are conducted with $p\text{CO}_2$ of 0.03 bar (*ExpH2outgassType1* in Table 3). The line colors represent different H_2 outgassing rates.

3.3. Response of Atmospheric $p\text{CH}_4$ to Biogenic CH_4 Supply Rate Variations

Next, we investigated the relationship between atmospheric $p\text{CH}_4$ and $\Phi_{\uparrow}(\text{CH}_4)$ using the photochemical model decoupled from the ecosystem model, to investigate the atmospheric response over a broader range of CH_4 flux values (Figure 6). Atmospheric $p\text{CH}_4$ responded nonlinearly to $\Phi_{\uparrow}(\text{CH}_4)$ variations for $\Phi_{\uparrow}(\text{CH}_4)$ values of 3–20 Tmol C yr^{-1} depending on atmospheric $p\text{CO}_2$. For example, for atmospheric $p\text{CO}_2$ equal to 0.1 bar, the atmospheric $p\text{CH}_4$ response becomes nonlinear for $\Phi_{\uparrow}(\text{CH}_4)$ values over approximately 6 Tmol C yr^{-1} (Figure 6a). To identify the main controlling factors for atmospheric $p\text{CH}_4$, we separated the chemical reactions consuming atmospheric CH_4 (Figure 6d, example for the case of $p\text{CO}_2 = 0.1$ bar). For $\Phi_{\uparrow}(\text{CH}_4)$ values lower than a threshold value of approximately 8 Tmol C yr^{-1} , reaction with OH radicals is the nearly exclusive atmospheric CH_4 consumption process. For higher flux values, photodissociation becomes dominant (Figure 6d).

For $\Phi_{\uparrow}(\text{CH}_4)$ values lower than the threshold value, the CH_4 –OH reaction rate is constrained by the CH_4 supply rate to the troposphere. Once the residing atmospheric CH_4 is consumed by reaction with OH, the relationship for CH_4 between its biogenic flux and volume mixing ratio (f_{CH_4}) is approximated by:

$$f_{\text{CH}_4} \approx \frac{\Phi_{\uparrow}(\text{CH}_4)}{\int_0^{z_{\text{crit}}} K \cdot n_{\text{OH}}(z) \cdot n_{\text{atm}}(z) \cdot dz}, \quad (6)$$

where $n_{\text{atm}}(z)$ and $n_{\text{OH}}(z)$ are the air and OH number densities at altitude z , K is the reaction rate constant, and z_{crit} is the maximum altitude below which CH_4 is well mixed ($z_{\text{crit}} \sim 60$ km). If n_{OH} is independent from $\Phi_{\uparrow}(\text{CH}_4)$, then f_{CH_4} and $\Phi_{\uparrow}(\text{CH}_4)$ should be linearly correlated.

When $\Phi_{\uparrow}(\text{CH}_4)$ approaches the threshold value, the CH_4 –OH reaction becomes less sensitive to $\Phi_{\uparrow}(\text{CH}_4)$ increases because the reaction rate is constrained by the availability of OH radicals in the troposphere (Figure 6d). As a result of consumption by biogenic CH_4 , the OH

surface mixing ratio decreases sharply. This confirms that the nonlinearity of the atmospheric $p\text{CH}_4$ response is directly related to OH and CH_4 abundance variations when $\Phi_1(\text{CH}_4)$ is above the threshold (Figure 6). Excess biogenic CH_4 that was not consumed in the troposphere is transported into the mesosphere and thermosphere, where it is photodissociated by strong solar ultraviolet (UV) radiation. This transition between chemical reactions regulating the atmospheric $p\text{CH}_4$ explains its nonlinear response to high biogenic CH_4 supply fluxes into the atmosphere.

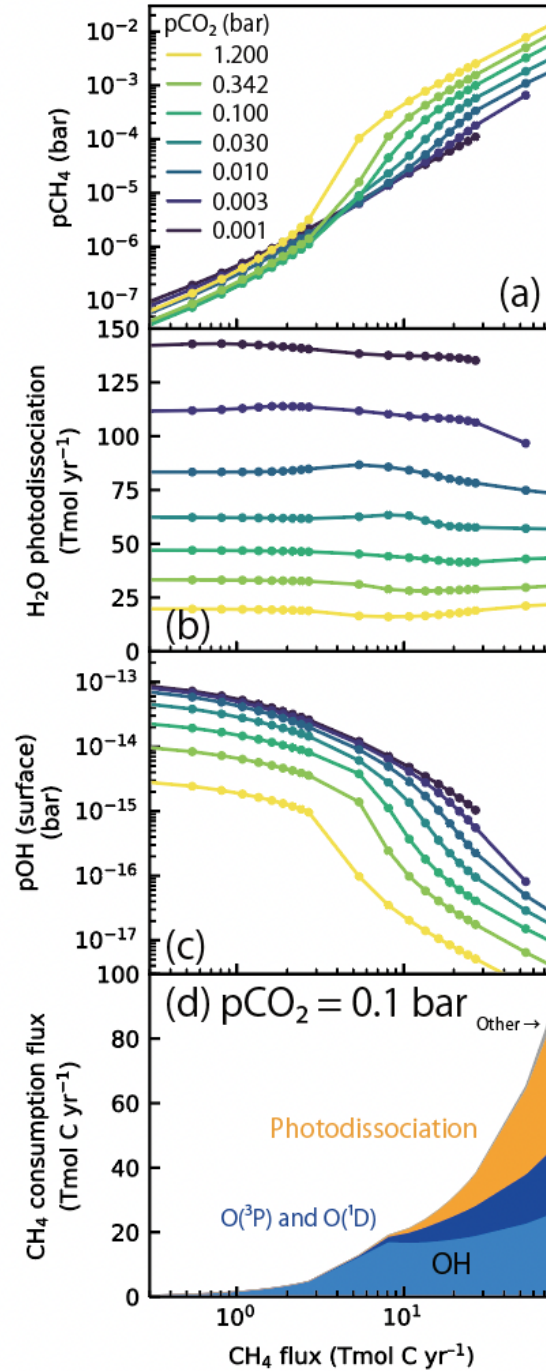


Figure 6. Changes in atmospheric $p\text{CH}_4$ (a), photodissociation rate of H_2O (b), partial pressure of OH at the surface (c), and the consumption pathway of the biogenic CH_4 flux to the atmosphere (d). Calculations are conducted with $p\text{CO}_2$ of 0.001, 0.003, 0.01, 0.03, 0.1, 0.342, and 1.2 bar ($\text{ExpCH}_4\text{flux}$ in Table 3). The line colors represent the atmospheric $p\text{CO}_2$. The result shown in (d) is for atmospheric $p\text{CO}_2$ of 0.1 bar.

3.4. Effect of Atmospheric $p\text{CO}_2$ Variations on CH_4 Amplification

The next set of simulations was designed to evaluate the dependence of atmospheric CH_4 abundances on $p\text{CO}_2$ (Figure 6, color-coding of curves in Panels a–c). The nonlinearity of the atmospheric $p\text{CH}_4$ response, explained in Section 3.3, increased with increasing atmospheric $p\text{CO}_2$, as illustrated in Figure 6, for example, for a $p\text{CO}_2$ value of 1.2 bar (Panel (a), yellow curve). Conversely, for a $p\text{CO}_2$ value of 0.001 bar, atmospheric $p\text{CH}_4$ depends nearly linearly on $\Phi_{\uparrow}(\text{CH}_4)$. We attribute this to the influence of atmospheric $p\text{CO}_2$ on tropospheric availability of OH radicals (Figure B1b). The source of tropospheric OH radicals is H_2O photodissociation (Figure 5h). Below the tropopause (approximately 10 km), the H_2O abundance is controlled by the adiabatic temperature gradient, which was fixed in these simulations. The H_2O photodissociation rate ($F_{\text{phot,H}_2\text{O}}$) is expressed as:

$$F_{\text{phot,H}_2\text{O}} = \int_z n_{\text{H}_2\text{O}}(z) \cdot \int_{\lambda} k_p(z, \lambda) d\lambda dz, \quad (7)$$

where $n_{\text{H}_2\text{O}}(z)$ is the H_2O number density at altitude z and $k_p(\lambda, z)$ is the photodissociation rate constant for H_2O , defined as:

$$k_p(\lambda, z) = \sigma(\lambda) \cdot \Phi(\lambda) \cdot F(\lambda, z), \quad (8)$$

where $\sigma(\lambda)$ is the H_2O absorption cross-section at wavelength λ , $\Phi(\lambda)$ is the quantum yield for H_2O photodissociation ($\Phi(\lambda) = 1$), and $F(\lambda, z)$ is the stellar irradiance.

Calculated wavelength-dependent k_p at the tropopause is plotted as a function of $p\text{CO}_2$ (color-coded curves) in Figure 7b. For an atmospheric $p\text{CO}_2$ value of 0.001 bar, the k_p value at the tropopause peaked at $\sim 170\text{--}210$ nm, indicating that tropospheric H_2O photodissociation is mainly controlled by solar irradiance in this wavelength range. When steady-state $p\text{CO}_2$ increases, the lower wavelength range limit increases, because of the shielding of the tropospheric H_2O by CO_2 . When $p\text{CO}_2$ reaches 0.03 bar, CO_2 almost completely absorbs the UV radiations at CO_2 absorption

bands. For higher values of atmospheric $p\text{CO}_2$, H_2O photodissociation only occurs within $\sim 200\text{--}210$ nm (Figure 7c). Therefore, the UV flux at $200\text{--}210$ nm is the dominant controlling factor for H_2O photodissociation, indicating that solar irradiance outside of this narrow spectral range does not strongly affect tropospheric H_2O photodissociation for $p\text{CO}_2$ values higher than 0.03 bar (Figure 7), hence that the H_2O photodissociation rate is inversely related to atmospheric $p\text{CO}_2$ (Figure 6b). This minimized OH availability in the troposphere and contributing to atmospheric CH_4 amplification, by inducing a nonlinear $p\text{CH}_4$ increase when atmospheric $p\text{CO}_2$ is sufficiently high to completely absorb solar radiation at $170\text{--}200$ nm.

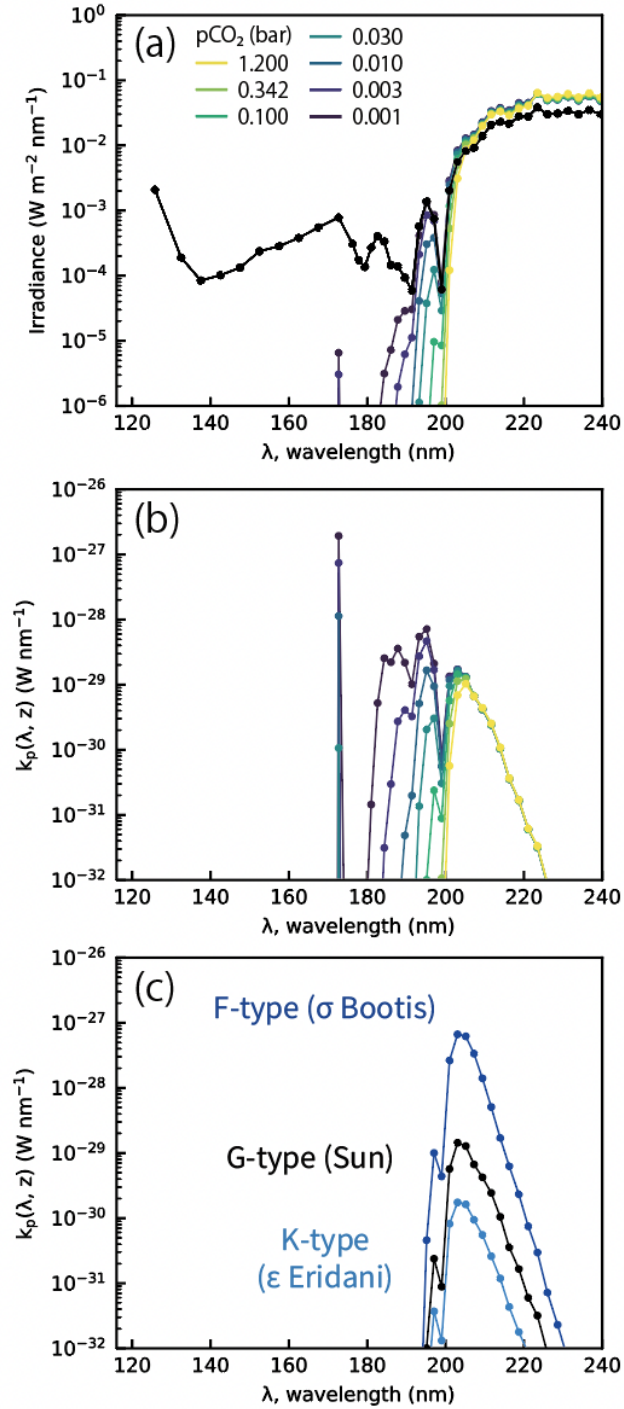


Figure 7. Irradiance at the top of the atmosphere (black) and at the troposphere (a) for the case of the early Earth (*ExpCH4flux* in Table 3). A rate constant for the photodissociation of H_2O at the tropopause (approximately 10 km) (b and c). The line colors represent the results with different atmospheric $p\text{CO}_2$ in (a) and (b), and the results using the spectrum of F-, G-, and K-type stars (blue, black, and light blue lines) (*ExpCH4fluxF2V*, *ExpCH4fluxG2V*, and *ExpCH4fluxK2V* in Table 3) in (c).

3.5. Effect of Stellar Spectra on CH₄ Amplification

Finally, we conducted several sets of simulations to analyze the dependence of $p\text{CH}_4$ on $\Phi_{\uparrow}(\text{CH}_4)$, as in Section 3.3, but under stellar irradiance conditions representative of three central star types (Section 2.2, Figure 2, and Table 3). Results are illustrated in Figure 8. The simulated atmospheric $p\text{CH}_4$ was lower with the F-type star spectrum than with the G-type star spectrum, but higher with the K-type star spectrum. We attribute this to stellar irradiance differences between F-, G-, and K-type stars. Specifically, the stellar irradiance at 200–210 nm, critical for H₂O photodissociation under high $p\text{CO}_2$ conditions (Section 3.4), was 10 times weaker and 40 times stronger (Figure 2) for the K-type and F-type stars, respectively, than for the G-type star (Sun). Such large irradiance discrepancies would critically affect the H₂O photodissociation rate, hence also atmospheric $p\text{CH}_4$. To confirm this, we repeated the G-type star simulation (with an atmospheric $p\text{CO}_2$ of 0.1 bar) but scaled the irradiance at approximately 200–210 nm relatively to its nominal value (Figure 2). For weaker stellar irradiances (0.5 and 0.1 times that of the G-type star), atmospheric $p\text{CH}_4$ increased and the $\Phi_{\uparrow}(\text{CH}_4)$ threshold value (nominally 8 Tmol C yr⁻¹, Section 3.3) decreased. This mechanism is also driven by variations in the tropospheric H₂O photodissociation rate, as discussed for early Earth in Section 3.4. Opposite variations are obtained for stronger stellar irradiances at 200–210 nm (2, 10, and 40 times that of the G-type star).

Simulation results for the 0.1 and 40 times scaling were comparable with those for the K- and F-type stars, respectively (Figure 8). Results for the K-type star yielded slightly higher atmospheric $p\text{CH}_4$ than for the G-type star with 0.1 times scaling, possibly because of the spectral properties of K-type stars at wavelengths shorter than 200 nm that potentially affect the CO₂ and CH₄ photodissociation rates. For low atmospheric $p\text{CO}_2$ (0.001 and 0.01 bar), the lower limit of the k_p peak wavelength range was 170 nm both for F- and K-type stars, similarly to the G-type star

simulations (Figure B2b and B2c). This similarity suggests that H₂O photodissociation is the primary control mechanism for atmospheric $p\text{CH}_4$, within a wide range of $p\text{CO}_2$ values, in the atmospheres of terrestrial exoplanets orbiting Sun-like stars (Figures B2–B3).

In the final set of simulations, we set the top-of-atmosphere solar irradiance by consecutively applying a global scaling factor (0.2–1.2 times the current Sun value) to the solar irradiance spectrum at all wavelengths, to simulate a range of conditions between the outer and inner edges of a habitable zone. Higher atmospheric $p\text{CH}_4$ (nearly one order of magnitude higher than on Earth, Figure 9) was calculated for the solar irradiance of 0.3 times the current value, representative of an exoplanet located farther from its central star near the outer edge of the habitable zone under the corresponding $\Phi_{\uparrow}(\text{CH}_4)$ value of $\sim 9.1 \text{ Tmol C yr}^{-1}$. By reducing the tropospheric H₂O photodissociation rate, the weaker stellar irradiance was directly responsible for the high simulated $p\text{CH}_4$, possibly indicating that planets orbiting near the outer edge of the habitable zone might be more suitably located to achieve high atmospheric $p\text{CH}_4$.

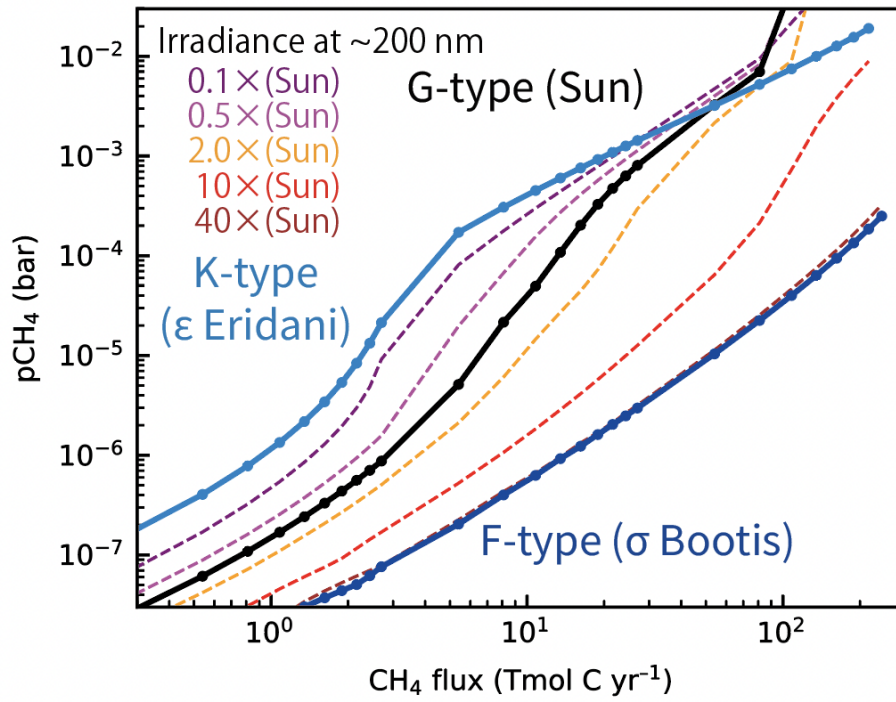


Figure 8. Responses of the atmospheric $p\text{CH}_4$ to biogenic CH_4 flux for the case of F-, G-, and K-type stars (blue, black, and light blue solid lines with dots) ($ExpCH_4fluxF2V$, $ExpCH_4fluxG2V$, and $ExpCH_4fluxK2V$ in Table 3). The dotted lines represent the results of the case of the G-type star with the scaled intensity of the spectra at 200–210 nm (0.1, 0.5, 2, 10, and 40 times for purple, light purple, orange, red, and brown lines, respectively). ($ExpCH_4flux200nm$ in Table 3).

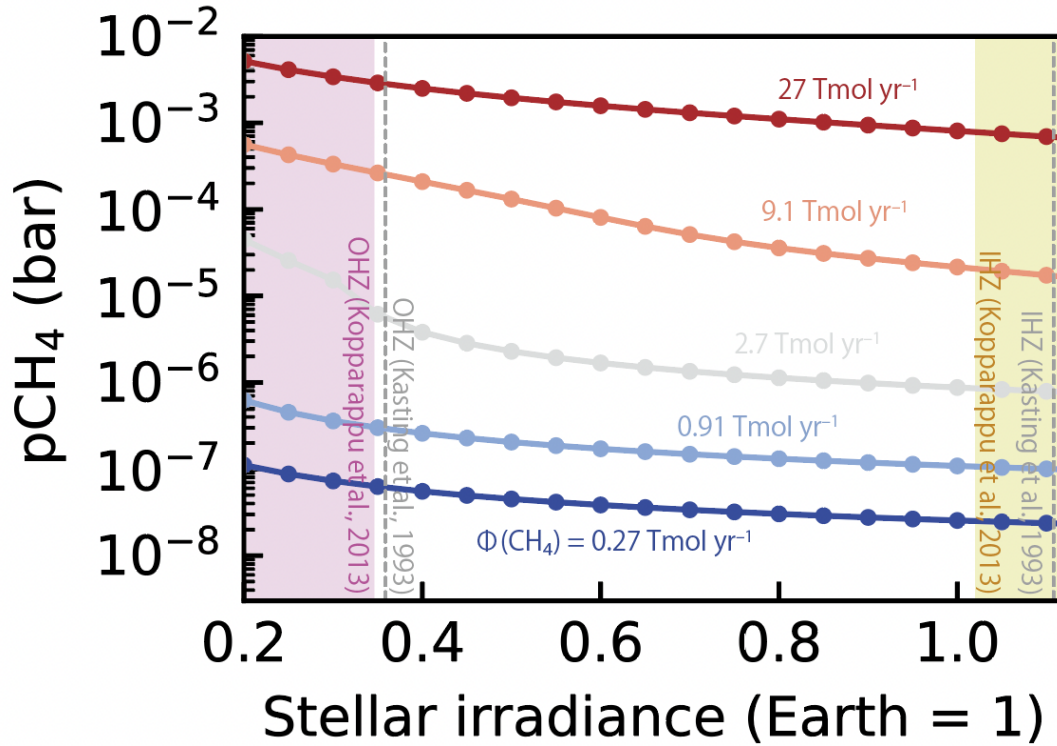


Figure 9. Responses of the atmospheric $p\text{CH}_4$ to biogenic CH_4 flux for the case of G-type star to different stellar irradiance (*ExpIrradiance* in Table 3). Different lines represent the different biogenic CH_4 fluxes (1×10^9 , 3×10^9 , 1×10^{10} , 3×10^{10} , and 1×10^{11} $\text{cm}^{-2} \text{s}^{-1}$ for blue, light blue, gray, light red, and red lines with dots, respectively). The vertical dashed lines represent the inner and outer edges of the habitable zone (IHZ and OHZ, respectively) estimated by Kasting et al. (1993). The yellow- and purple-hatched regions represent the condition inside the IHZ and the outside the OHZ estimated by Kopparapu et al. (2013), respectively.

4. DISCUSSION

In this study, we evaluated the relationships between flux of reducing power to the ocean–atmosphere system (H_2 and CO outgassing fluxes and Fe(II) supply flux), $\Phi_{\uparrow}(\text{CH}_4)$ to the atmosphere, and atmospheric $p\text{CH}_4$, by applying our coupled atmospheric photochemistry–primitive marine microbial ecosystem model to the early Earth. Our results demonstrate that CO–C activities are a major factor relating an influx of reducing power to $\Phi_{\uparrow}(\text{CH}_4)$. The effect of a nonlinear increase in atmospheric CO is further enhanced by a decrease in the OH concentration. Moreover, we showed that the tropospheric OH availability is primarily controlled by H_2O photodissociation and, in turn, controls atmospheric $p\text{CH}_4$. Consequently, atmospheric $p\text{CH}_4$ is affected by atmospheric $p\text{CO}_2$ variations via changing H_2O photodissociation rate and the availability of OH radicals. More specifically, the solar irradiance at $\sim 200\text{--}210$ nm is the primarily controlling factor for the H_2O photodissociation when atmospheric $p\text{CO}_2$ exceeds ~ 0.03 bar. It is expected that atmospheric $p\text{CO}_2$ should show a long-term decreasing trend, explained by adjustments of the carbonate-silicate geochemical cycle to a decrease in the CO_2 outgassing rate from interior of the Earth and to increases in solar luminosity and land fraction (Walker et al. 1981; Tajika and Matsui 1992; Kasting 1993; Krissansen-Totton et al. 2018; Kadoya and Tajika 2019; Kadoya et al. 2020; Watanabe and Tajika 2021; Watanabe et al. 2023a). Accordingly, nonlinear atmospheric $p\text{CH}_4$ amplification likely occurred more easily during the early Archean after the emergence of life. Additionally, early-Earth outgassing rates for reducing gases were likely higher than their current value (Holland 1984; Krissansen-Totton et al. 2018, 2021). Such conditions are suitable for nonlinear amplification of atmospheric CH_4 on early Earth that probably occurred immediately after a primitive marine biosphere emerged. However, although OH availability is also affected by tropospheric temperature, which demonstrably influences tropospheric H_2O

concentrations, this temperature effect was not considered in this study; instead, a fixed atmospheric temperature vertical profile was used. When atmospheric $p\text{CO}_2$ is high, surface temperature increases and more OH radicals than simulated in this study are produced in the troposphere. Therefore, the results with our high- $p\text{CO}_2$ analysis represent an upper limit to the estimated atmospheric $p\text{CH}_4$ values. Nevertheless, we do not expect a strong effect on atmospheric $p\text{CH}_4$ because early-Earth climatic conditions would have been regulated by the carbonate-silicate geochemical cycle.

We also explored the effect of stellar irradiance on the atmospheric $p\text{CH}_4$ variations for Earth-like inhabited exoplanets, both depending on their location inside the habitable zone and on the central star. Our results show that exoplanetary atmospheric $p\text{CH}_4$ variations are also strongly controlled by the stellar spectrum intensity. Inhabited exoplanets around K-type stars would exhibit markedly higher atmospheric $p\text{CH}_4$ than F- or G-type stars, providing optimal conditions to search for life (Grenfell et al. 2007; Arney 2019). Conversely, the strong stellar irradiance provided by F-type stars would likely prevent a strong buildup of atmospheric $p\text{CH}_4$ on their planets.

Furthermore, we demonstrated that inhabited exoplanets orbiting near the outer edge of the habitable zone are more likely to exhibit high atmospheric $p\text{CH}_4$ because the correspondingly weaker stellar irradiance would enhance atmospheric $p\text{CO}_2$ through the carbonate-silicate geochemical cycle (Kadoya and Tajika 2014, 2019), inducing an increase in atmospheric $p\text{CH}_4$. In such a case, tropospheric H_2O photodissociation and atmospheric $p\text{CH}_4$ would be strongly controlled by the 200–210 nm stellar irradiance under high atmospheric $p\text{CO}_2$ conditions. This would also provide an ideal setting to produce high atmospheric $p\text{CH}_4$ (Grenfell et al. 2007). Planets orbiting Sun-like stars near the outer edge of their habitable zone are less likely to present

a false positive O₂ biosignature (Meadows 2017). Thus, they are optimally suited to search for extraterrestrial life. Incidentally, high atmospheric $p\text{CO}_2$ conditions, promoted by the limited stellar irradiance at the outer edge of the habitable zone, may also affect the exoplanetary atmospheric composition through the formation of CO₂ clouds in the polar regions (Kasting 1991; Pierrehumbert and Erlick 1998).

Conversely, near the inner edge of the habitable zone (solar irradiance of 1.01–1.10 times that of the current Sun) (Kasting et al. 1993; Kopparapu et al. 2013), atmospheric $p\text{CH}_4$ is comparable with standard G-type star irradiance, but marginally lower. In this case, steady-state atmospheric $p\text{CH}_4$ should be considerably smaller (Grenfell et al. 2007), because the higher surface temperature would yield a larger tropospheric H₂O abundance than that inferred from the input profile adopted in this study. Therefore, a comprehensive approach combining a global carbon cycle model, a climate model, a photochemical model, and a marine microbial ecosystem model is essential to better constraining atmospheric $p\text{CH}_4$ in exoplanetary atmospheres orbiting within the habitable zone of Sun-like stars. For exoplanets orbiting the M-type stars, which is not explored in this study, spectra of the stellar irradiance at ultraviolet wavelengths would be different from those of Sun-like stars. The controlling factor of atmospheric $p\text{CH}_4$ on exoplanets around M-type stars should also be investigated in future studies.

5. CONCLUSION

In this study, we investigated controlling factors influencing the atmospheric CH₄ abundance of early Earth and of potentially inhabited Earth-like exoplanets orbiting Sun-like stars (F-, G-, and K-type), using a 1D atmospheric photochemical model and a primitive marine microbial

ecosystem model. Nonlinear amplification of the early-Earth $\Phi_{\uparrow}(\text{CH}_4)$ into the atmosphere is explained primarily by an amplification of the atmospheric CO cycle and by the activity of CO-C. The nonlinear atmospheric $p\text{CH}_4$ response to $\Phi_{\uparrow}(\text{CH}_4)$ variations is caused by a decrease in the H_2O photodissociation rate. Atmospheric CH_4 abundances on inhabited Earth-like exoplanets orbiting Sun-like stars are mainly controlled by $\Phi_{\uparrow}(\text{CH}_4)$ and stellar irradiance. Potentially inhabited Earth-like exoplanets orbiting K-type stars near the outer edge of their habitable zone would be a suitable candidate for detection of CH_4 biosignatures.

6. Acknowledgments

This work is supported by Grant-in-aid for JSPS Research Fellow Number 20J12951 (YW). We thank Kazumi Ozaki for fruitful discussions. We thank Eric Dupuy, Ph.D., from Edanz (<https://jp.edanz.com/ac>) for editing a draft of this manuscript.

7. Competing interest

The authors declare no competing interest.

References

- Arney G, Domagal-Goldman SD, Meadows VS, et al (2016) The Pale Orange Dot: The Spectrum and Habitability of Hazy Archean Earth. *Astrobiology* 16:873–899
- Arney G, Domagal-Goldman SD, Meadows VS (2018) Organic Haze as a Biosignature in Anoxic Earth-like Atmospheres. *Astrobiology* 18:311–329
- Arney GN (2019) The K Dwarf advantage for biosignatures on directly imaged exoplanets. *Astrophysical Journal Letters* 873:L7
- Arney GN, Meadows VS, Domagal-Goldman SD, et al (2017) Pale Orange Dots: The Impact of Organic Haze on the Habitability and Detectability of Earthlike Exoplanets. *Astrophys J* 836:1–19
- Battistuzzi FU, Feijao A, Hedges SB (2004) A genomic timescale of prokaryote evolution: insights into the origin of methanogenesis, phototrophy, and the colonization of land. *BMC Evol Biol* 4:44

- Betts JN, Holland HD (1991) The oxygen content of ocean bottom waters, the burial efficiency of organic carbon, and the regulation of atmospheric oxygen. *Glob Planet Change* 97:5–18
- Canfield DE, Rosing MT, Bjerrum C (2006) Early anaerobic metabolisms. *Philos Trans R Soc Lond B Biol Sci* 361:1819–1836
- Catling DC, Kasting JF (2017) *Atmospheric evolution on inhabited and lifeless worlds*. Cambridge University Press
- Catling DC, Krissansen-Totton J, Kiang NY, et al (2018) Exoplanet Biosignatures: A Framework for Their Assessment. *Astrobiology* 18:709–738
- Catling DC, Zahnle KJ (2020) The Archean atmosphere. *Sci Adv* 6:eaax1420
- Chyba CF, McDonald GD (1995) The origin of life in the solar system: current issues. *Annu Rev Earth Planet Sci* 23:215–249
- Dodd MS, Papineau D, Grenne T, et al (2017) Evidence for early life in Earth's oldest hydrothermal vent precipitates. *Nature* 543:60–64
- Feulner G (2012) The faint young Sun problem. *Reviews of Geophysics* 50.:
<https://doi.org/10.1029/2011rg000375>
- Goldblatt C, Zahnle KJ (2011) Clouds and the Faint Young Sun Paradox. *Climate of the Past* 7:203–220
- Gough DO (1981) Solar Interior Structure and Luminosity Variations. In: Domingo V (ed) *Physics of Solar Variations*. Springer Netherlands, Dordrecht, pp 21–34
- Grenfell JL, Stracke B, von Paris P, et al (2007) The response of atmospheric chemistry on earthlike planets around F, G and K Stars to small variations in orbital distance. *Planet Space Sci* 55:661–671
- Haqq-Misra JD, Domagal-Goldman SD, Kasting PJ, Kasting JF (2008) A revised, hazy methane greenhouse for the Archean Earth. *Astrobiology* 8:1127–1137
- Holland HD (1984) *The chemical evolution of the atmosphere and oceans*. Princeton University Press
- Isson TT, Planavsky NJ (2018) Reverse weathering as a long-term stabilizer of marine pH and planetary climate. *Nature* 560:471–475
- Kadoya S, Krissansen-Totton J, Catling DC (2020) Probable cold and alkaline surface environment of the Hadean Earth caused by impact ejecta weathering. *Geochem Geophys Geosyst* 21:e2019GC008734
- Kadoya S, Tajika E (2019) Outer Limits of the Habitable Zones in Terms of Climate Mode and Climate Evolution of Earth-like Planets. *ApJ* 875:7
- Kadoya S, Tajika E (2014) Conditions for oceans on Earth-like planets orbiting within the habitable zone: importance of volcanic CO₂ degassing. *ApJ* 790:107
- Kanzaki Y, Murakami T (2015) Estimates of atmospheric CO₂ in the Neoproterozoic–Paleoproterozoic from paleosols. *Geochimica et Cosmochimica Acta* 159:190–219
- Kasting J (2005) Methane and climate during the Precambrian era. *Precambrian Research* 137:119–129

- Kasting JF (1993) Earth's early atmosphere. *Science* 259:920–926
- Kasting JF (1991) CO₂ condensation and the climate of early Mars. *Icarus* 94:1–13
- Kasting JF, Catling D (2003) Evolution of a Habitable Planet. *Annu Rev Astron Astrophys* 41:429–463
- Kasting JF, Whitmire DP, Reynolds RT (1993) Habitable zones around main sequence stars. *Icarus* 101:108–128
- Kharecha P, Kasting J, Siefert J (2005) A coupled atmosphere-ecosystem model of the early Archean Earth. *Geobiology* 3:53–76
- Kiehl JT, Dickinson RE (1987) A study of the radiative effects of enhanced atmospheric CO₂ and CH₄ on early Earth surface temperatures. *J Geophys Res* 92:2991–2998
- Kopparapu RK, Ramirez R, Kasting JF, et al (2013) Habitable zones around main-sequence stars: new estimates. *The Astrophysical Journal* 765:131
- Kopparapu RK, Ramirez RM, SchottelKotte J, et al (2014) Habitable zones around main-sequence stars: dependence on planetary mass. *The Astrophysical Journal Letters* 787:L29
- Krissansen-Totton J, Arney GN, Catling DC (2018) Constraining the climate and ocean pH of the early Earth with a geological carbon cycle model. *Proc Natl Acad Sci U S A* 115:4105–4110
- Krissansen-Totton J, Kipp MA, Catling DC (2021) Carbon cycle inverse modeling suggests large changes in fractional organic burial are consistent with the carbon isotope record and may have contributed to the rise of oxygen. *Geobiology* 19:342–363
- Krissansen-Totton J, Thompson M, Galloway ML, Fortney JJ (2022) Understanding planetary context to enable life detection on exoplanets and test the Copernican principle. *Nature Astronomy* 6:189–198
- Lazcano A, Miller SL (1994) How long did it take for life to begin and evolve to cyanobacteria? *J Mol Evol* 39:546–554
- Meadows VS (2017) Reflections on O₂ as a Biosignature in Exoplanetary Atmospheres. *Astrobiology* 17:1022–1052
- Mojzsis SJ, Harrison TM, Pidgeon RT (2001) Oxygen-isotope evidence from ancient zircons for liquid water at the Earth's surface 4,300 Myr ago. *Nature* 409:178–181
- Ozaki K, Tajika E, Hong PK, et al (2018) Effects of primitive photosynthesis on Earth's early climate system. *Nature Geoscience* 11:55–59
- Pavlov AA, Brown LL, Kasting JF (2001) UV shielding of NH₃ and O₂ by organic hazes in the Archean atmosphere. *Journal of Geophysical Research: Planets* 106:23267–23287
- Pavlov AA, Hurtgen MT, Kasting JF, Arthur MA (2003) Methane-rich Proterozoic atmosphere? *Geology* 31:87
- Pearce BKD, Tupper AS, Pudritz RE, Higgs PG (2018) Constraining the Time Interval for the Origin of Life on Earth. *Astrobiology* 18:343–364

- Pierrehumbert RT, Erlick C (1998) On the scattering greenhouse effect of CO₂ ice clouds. *Journal of the Atmospheric Sciences* 55:1897–1903
- Ragsdale SW (2004) Life with carbon monoxide. *Crit Rev Biochem Mol Biol* 39:165–195
- Ranjan S, Schwieterman EW, Harman C, et al (2020) Photochemistry of anoxic abiotic habitable planet atmospheres: impact of new H₂O cross sections. *The Astrophysical Journal* 896:148
- Ranjan S, Seager S, Zhan Z, et al (2022) Photochemical Runaway in Exoplanet Atmospheres: Implications for Biosignatures. *The Astrophysical Journal* 930:131
- Sagan C, Chyba C (1997) The early faint sun paradox: organic shielding of ultraviolet-labile greenhouse gases. *Science* 276:1217–1221
- Sagan C, Mullen G (1972) Earth and Mars: Evolution of Atmospheres and Surface Temperatures. *Science* 177:52–56
- Sauterey B, Charnay B, Affholder A, et al (2020) Co-evolution of primitive methane-cycling ecosystems and early Earth's atmosphere and climate. *Nature communications* 11:2705
- Schindler TL, Kasting JF (2000) Synthetic spectra of simulated terrestrial atmospheres containing possible biomarker gases. *Icarus* 145:262–271
- Schwieterman EW, Reinhard CT, Olson SL, et al (2019) Rethinking CO Antibiosignatures in the Search for Life Beyond the Solar System. *The Astrophysical Journal* 874:9
- Segura A, Krelove K, Kasting JF, et al (2003) Ozone concentrations and ultraviolet fluxes on Earth-like planets around other stars. *Astrobiology* 3:689–708
- Selsis F, Kasting JF, Levrard B, et al (2007) Habitable planets around the star Gliese 581? *Astron Astrophys Suppl Ser* 476:1373–1387
- Tajika E, Matsui T (1992) Evolution of terrestrial proto-CO₂ atmosphere coupled with thermal history of the earth. *Earth and Planetary Science Letters* 113:251–266
- Tashiro T, Ishida A, Hori M, et al (2017) Early trace of life from 3.95 Ga sedimentary rocks in Labrador, Canada. *Nature* 549:516–518
- Thompson MA, Krissansen-Totton J, Wogan N, et al (2022) The case and context for atmospheric methane as an exoplanet biosignature. *Proc Natl Acad Sci U S A* 119:e2117933119
- Thuillier G, Floyd L, Woods TN, et al (2004) Solar irradiance reference spectra for two solar active levels. *Adv Space Res* 34:256–261
- Ueno Y, Yamada K, Yoshida N, et al (2006) Evidence from fluid inclusions for microbial methanogenesis in the early Archaean era. *Nature* 440:516–519
- Walker JCG, Hays PB, Kasting JF (1981) A negative feedback mechanism for the long-term stabilization of Earth's surface temperature. *J Geophys Res* 86:9776
- Ward LM, Rasmussen B, Fischer WW (2019) Primary productivity was limited by electron donors prior to the advent of oxygenic photosynthesis. *J Geophys Res Biogeosci* 124:211–226

- Watanabe Y, Ozaki K (2023) Relative abundances of CO₂, CO, and CH₄ in atmospheres of Earth-like lifeless planets. arXiv [astro-ph.EP]
- Watanabe Y, Tajika E (2021) Atmospheric oxygenation of the early earth and earth-like planets driven by competition between land and seafloor weathering. *Earth Planets Space* 73:1–10
- Watanabe Y, Tajika E, Ozaki K (2023a) Evolution of iron and oxygen biogeochemical cycles during the Precambrian. *Geobiology* 21:689–707
- Watanabe Y, Tajika E, Ozaki K (2023b) Biogeochemical transformations after the emergence of oxygenic photosynthesis and conditions for the first rise of atmospheric oxygen. *Geobiology* 21:537–555
- Wilde SA, Valley JW, Peck WH, Graham CM (2001) Evidence from detrital zircons for the existence of continental crust and oceans on the Earth 4.4 Gyr ago. *Nature* 409:175–178
- Wogan NF, Catling DC (2020) When is Chemical Disequilibrium in Earth-like Planetary Atmospheres a Biosignature versus an Anti-biosignature? *Disequilibria from Dead to Living Worlds. Astrophys J* 892:127
- Wogan N, Krissansen-Totton J, Catling DC (2020) Abundant Atmospheric Methane from Volcanism on Terrestrial Planets Is Unlikely and Strengthens the Case for Methane as a Biosignature. *The Planetary Science Journal* 1:58
- Wolfe JM, Fournier GP (2018) Horizontal Gene Transfer Constrains the Timing of Methanogen Evolution. *Cold Spring Harbor Laboratory* 129494
- Wordsworth R, Pierrehumbert R (2013) Hydrogen-nitrogen greenhouse warming in Earth's early atmosphere. *Science* 339:64–67

APPENDIX A

The absorption cross-section of CO₂ and H₂O employed in this study is shown in Figure A1.

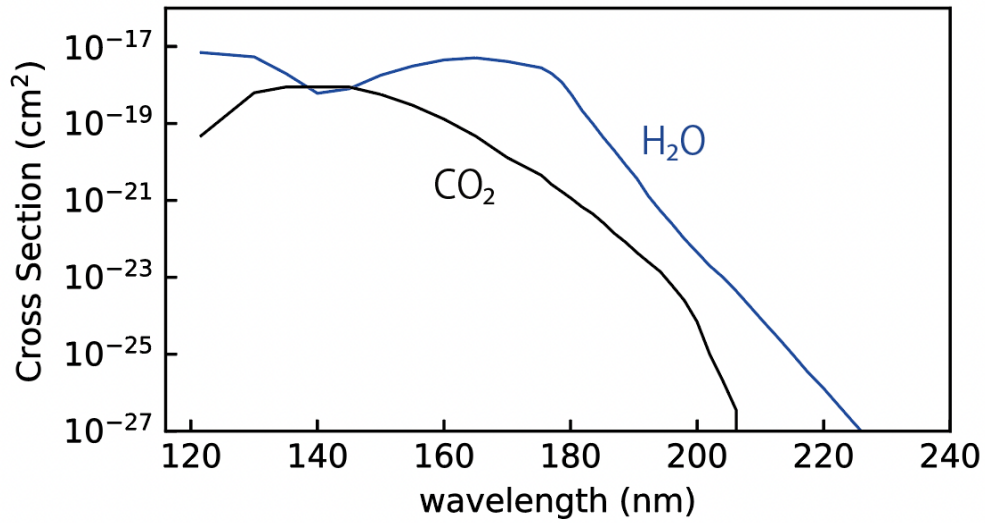


Figure A1. Absorption cross-section of CO₂ and H₂O adopted in this study.

APPENDIX B

The vertical profiles of atmospheric species and reaction rates with respect to different atmospheric $p\text{CO}_2$ are shown in Figure B1. The rate constants for the photodissociation of H_2O at the tropopause (10 km) and atmospheric $p\text{CH}_4$ for different atmospheric $p\text{CO}_2$ values and central stars are shown in Figures B2 and B3, respectively.

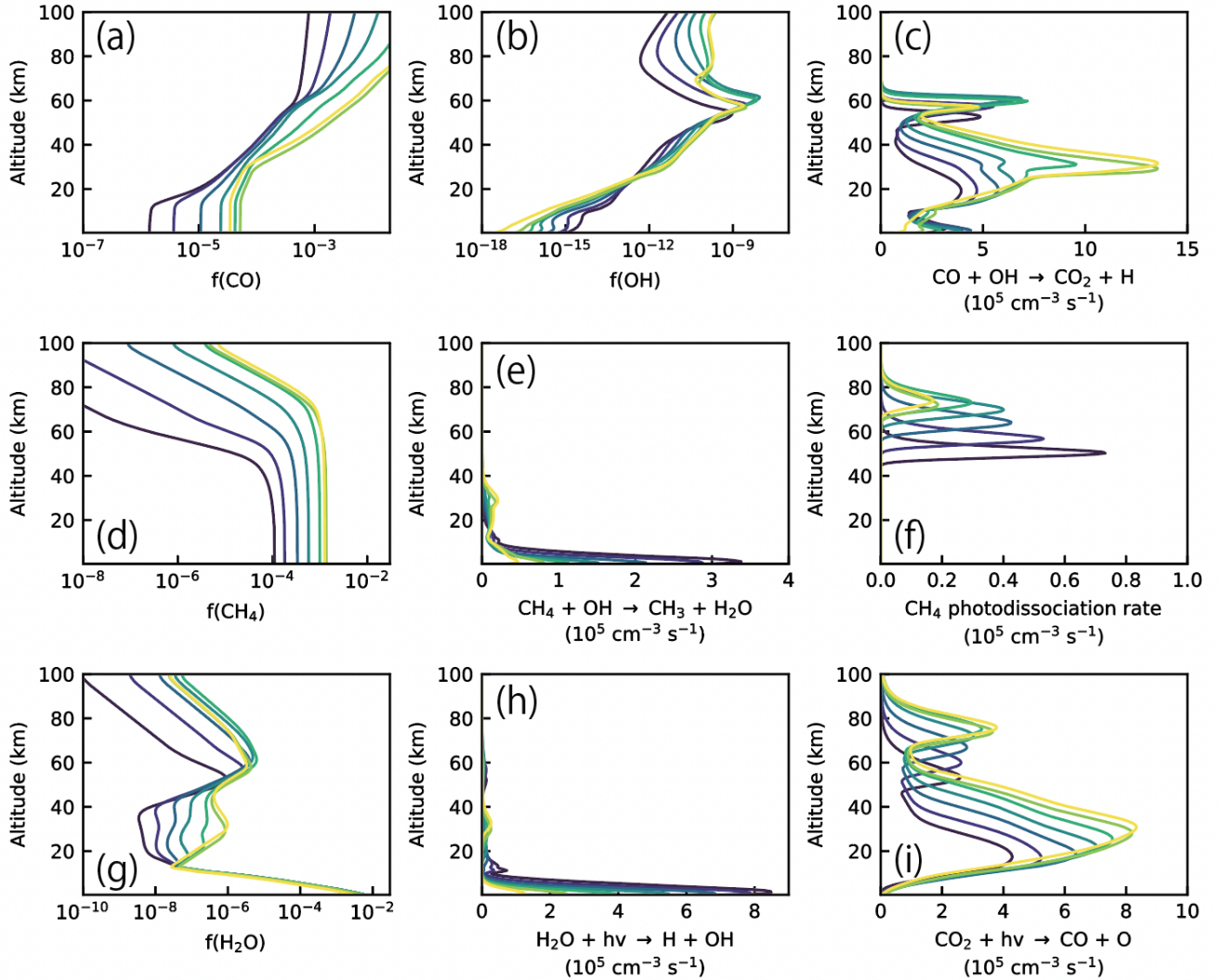


Figure B1. Vertical profiles of the atmospheric components and the reaction rates. Vertical profiles of (a) CO mixing ratio, (b) OH radical mixing ratio, (c) reaction rate of $\text{CO} + \text{OH} \rightarrow \text{CO}_2 + \text{H}$, (d) CH_4 mixing ratio, reaction rate of (e) $\text{CH}_4 + \text{OH} \rightarrow \text{CH}_3 + \text{H}_2\text{O}$, (f) photodissociation rate of CH_4 , (g) H_2O mixing ratio, (h) photodissociation rate of H_2O , and (i) photodissociation rate of CO_2 . Calculations are conducted with different atmospheric $p\text{CO}_2$ and a fixed CH_4 flux ($2.7 \text{ Tmol C yr}^{-1}$) (*ExpCH4flux* in Table 3). The line colors represent atmospheric $p\text{CO}_2$ (0.001, 0.003, 0.01, 0.03, 0.1, 0.342, and 1.2 bar).

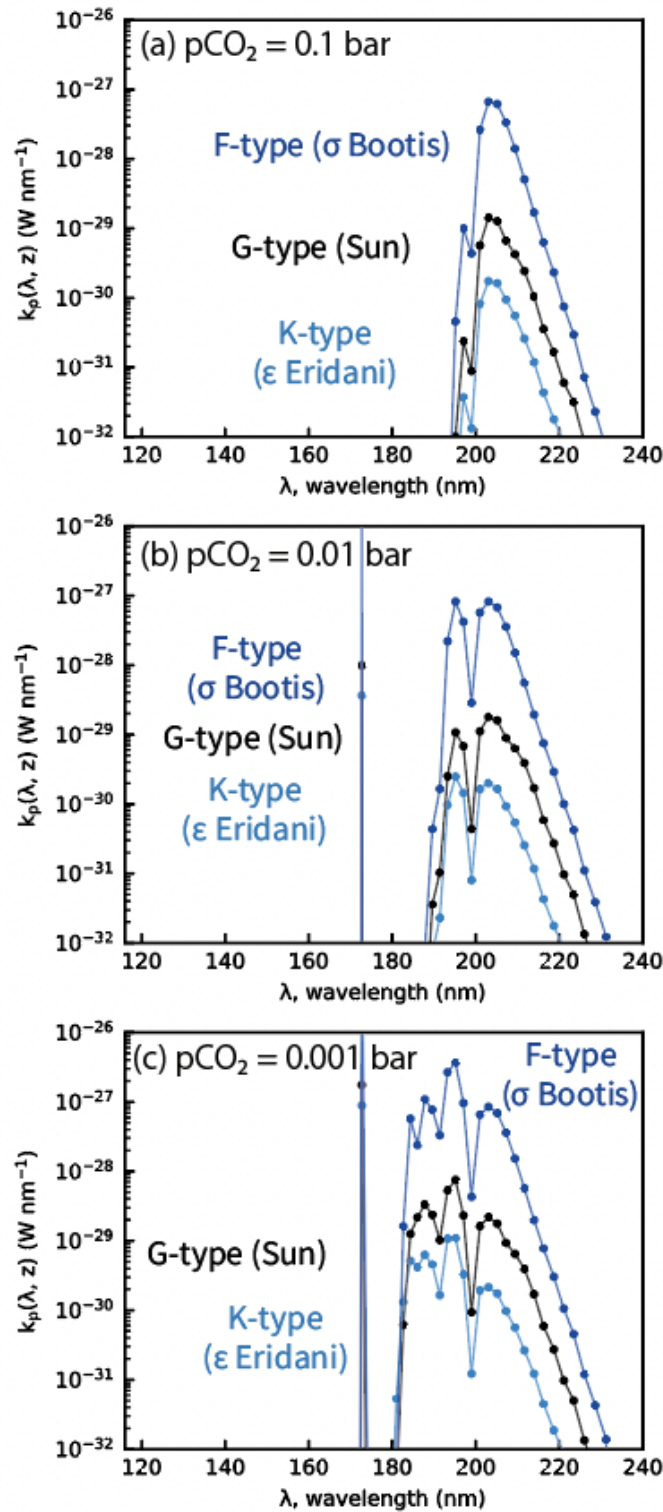


Figure B2. Rate constants for the photodissociation of H_2O at the tropopause (approximately 10 km) for different atmospheric $p\text{CO}_2$ (0.1, 0.01, and 0.001 bar for a, b, and c, respectively). The line colors represent the results using the spectrum of F-, G-, and K-type stars (blue, black, and light blue lines) (*ExpCH4fluxF2V*, *ExpCH4fluxG2V*, and *ExpCH4fluxK2V* in Table 3).

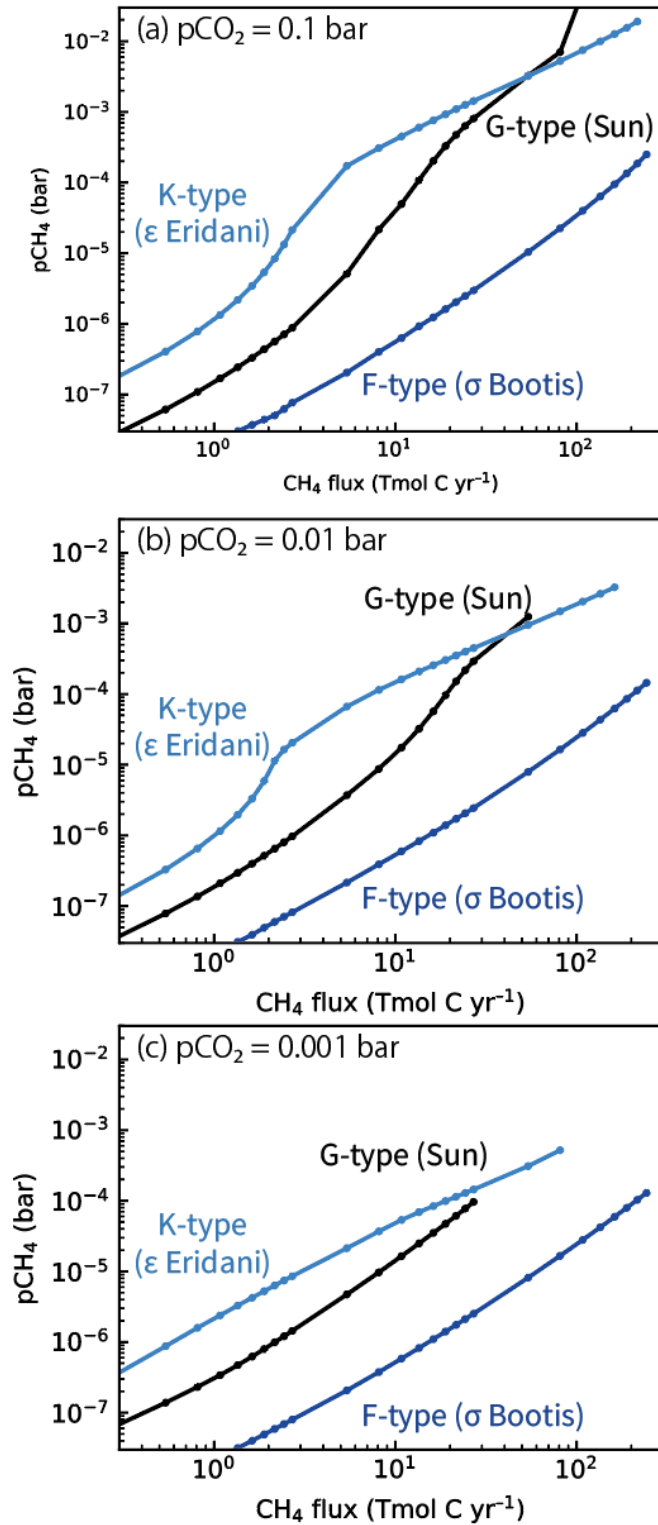


Figure B3. Responses of the atmospheric $p\text{CH}_4$ to biogenic CH_4 flux for the case of F-, G-, and K-type stars (blue, black, and light blue solid lines with dots) ($Exp\text{CH}_4\text{fluxF2V}$, $Exp\text{CH}_4\text{fluxG2V}$, and $Exp\text{CH}_4\text{fluxK2V}$ in Table 3) calculated with the atmospheric $p\text{CO}_2$ of 0.1, 0.01, and 0.001 bar (a, b, and c, respectively).